May 28th, 2021

Star Formation Newsletter No.340 #27-35

Shota Notsu (RIKEN)

- 27: Magnetic Properties of Star-Forming Dense Cores
- 28: Testing the Turbulent Origin of the Stellar Initial Mass Function
- **29: X-ray induced chemistry of water and related molecules in low-mass protostellar envelopes**
- **30: The double signature of local cosmic-ray acceleration in star-forming regions**
- 31: Modulated accretion in T Tauri star RY Tau -- stable MHD propeller or a planet at 0.2 AU?
- **32: Significant interstellar object production by close stellar flybys**
- 33: Thiols in the ISM: first detection of HC(O)SH and confirmation of C2H5SH
- **34: The effect of the streaming instability on protoplanetary disc emission at millimetre wavelengths**
- 35: Gaia-EDR3 Parallax Distances to the Great Carina Nebula and its Star Clusters (Trumpler 14, 15, 16)

https://arxiv.org/abs/2104.06878v1

29. X-ray induced chemistry of water and related molecules in low-mass protostellar envelopes

Shota Notsu, Ewine F. van Dishoeck, Catherine Walsh, Arthur D. Bosman, Hideko Nomura

★ Recent water line observations toward several low-mass protostars suggest low water gas fractional abundances in the inner warm envelopes. Water destruction by X-rays has been proposed to influence the water abundances in these regions, but the detailed chemistry, including the nature of alternative oxygen carriers, is not yet understood. In this study, we aim to understand the impact of X-rays on the composition of low-mass protostellar envelopes, focusing specifically on water and related oxygen bearing species. We compute the chemical composition of two low-mass protostellar envelopes using a 1D gas-grain chemical reaction network, under various X-ray field strengths. According to our calculations, outside the water snowline, the water gas abundance increases with $L_{\rm X}$. Inside the water snowline, water maintains a high abundance of $\sim 10^{-4}$ for small $L_{\rm X}$, with water and CO being the dominant oxygen carriers. For large $L_{\rm X}$, the water gas abundances significantly decrease just inside the water snowline (down to $\sim 10^{-8} - 10^{-7}$) and in the innermost regions ($\sim 10^{-6}$). For these cases, the O_2 and O gas abundances reach $\sim 10^{-4}$ within the water snowline, and they become the dominant oxygen carriers. The HCO^+ and CH_3OH abundances, which have been used as tracers of the water snowline, significantly increase/decrease within the water snowline, respectively, as the X-ray fluxes become larger. The abundances of some other dominant molecules, such as CO_2, OH, CH_4, HCN, and NH_3, are also affected by strong X-ray fields, especially within their own snowlines. These X-ray effects are larger in lower density envelope models. Future observations of water and related molecules (using e.g., ALMA and ngVLA) will access the regions around protostars where such X-ray induced chemistry is effective.

低質量Class 0原始星周りのエンベロープの詳細な化学構造計算を実施
原始星エンベロープの分子組成に対する、中心星 X 線放射の影響を調査

Notsu et al. (2021, A&A in press.)

中心星X線放射によるH_2Oガス分子の破壊?

Persson et al. (2016), Harsono et al. (2020)

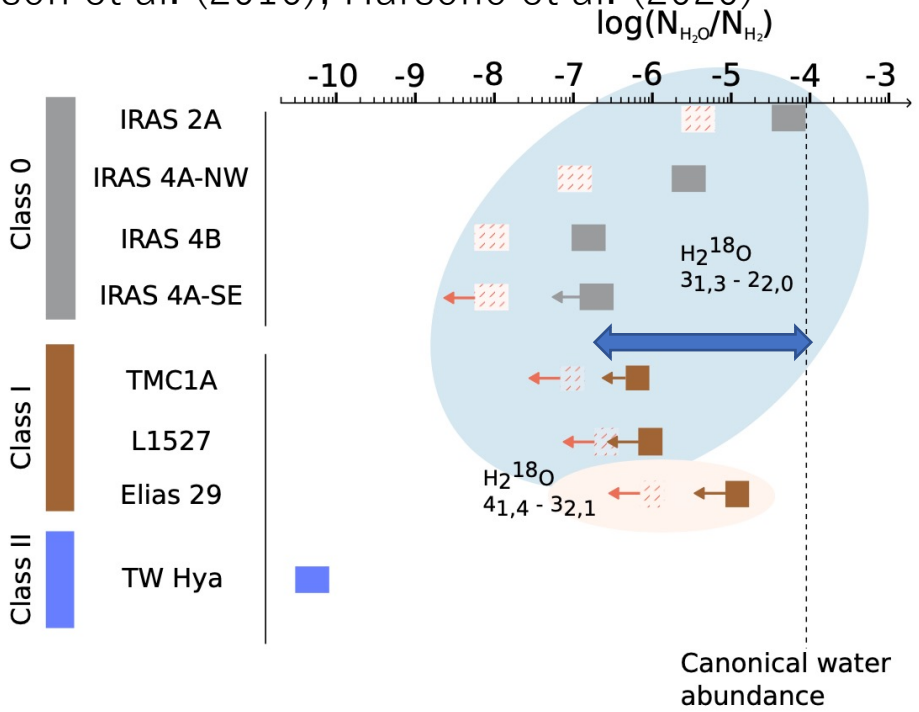

先行研究：Stauber et al. (2005, 2006)

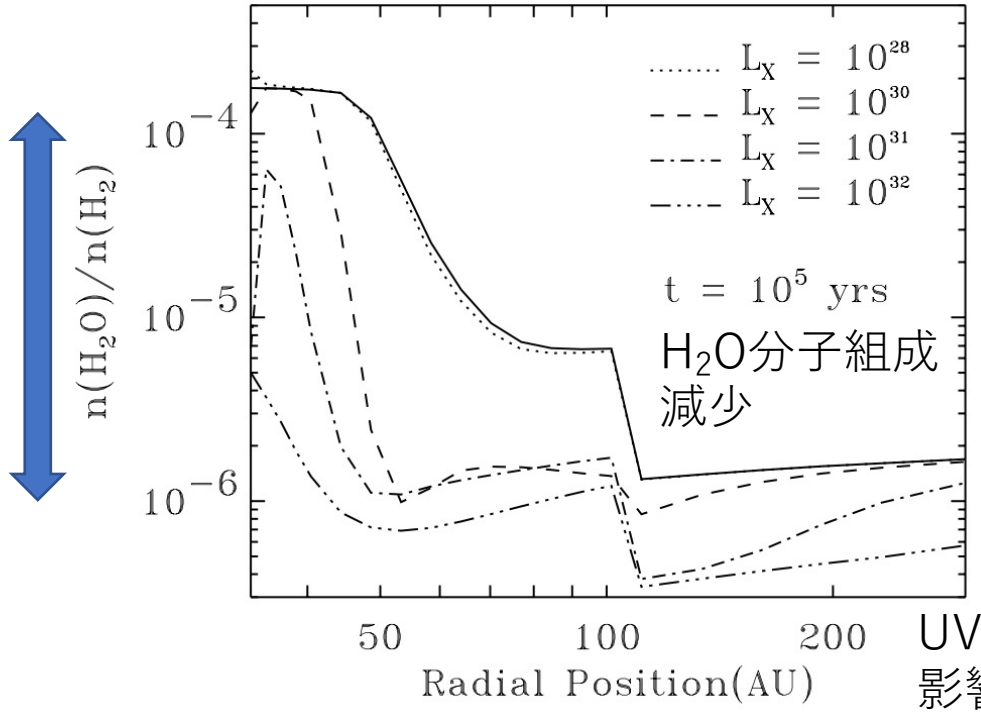

UV放射の影響は小さい

一部の低質量原始星エンベロープ&円盤の内縁高温部で、H_2O分子組成が著しく減少($<10^{-6}$)！

↓

中心星X線放射によるH_2O分子の破壊が効いている?

<u>先行研究の課題</u>

-化学反応計算が不十分。特に、ダスト表面反応や非熱的なダスト・ガス相互作用などが入っていない

-H_2O分子以外の関連分子の振る舞い、特に酸素原子の担い手を解明したい

→詳細な化学構造計算を実施 (Notsu et al. 2021)

低質量原始星エンベロープのH_2Oガス&氷組成

Notsu et al. (2021)

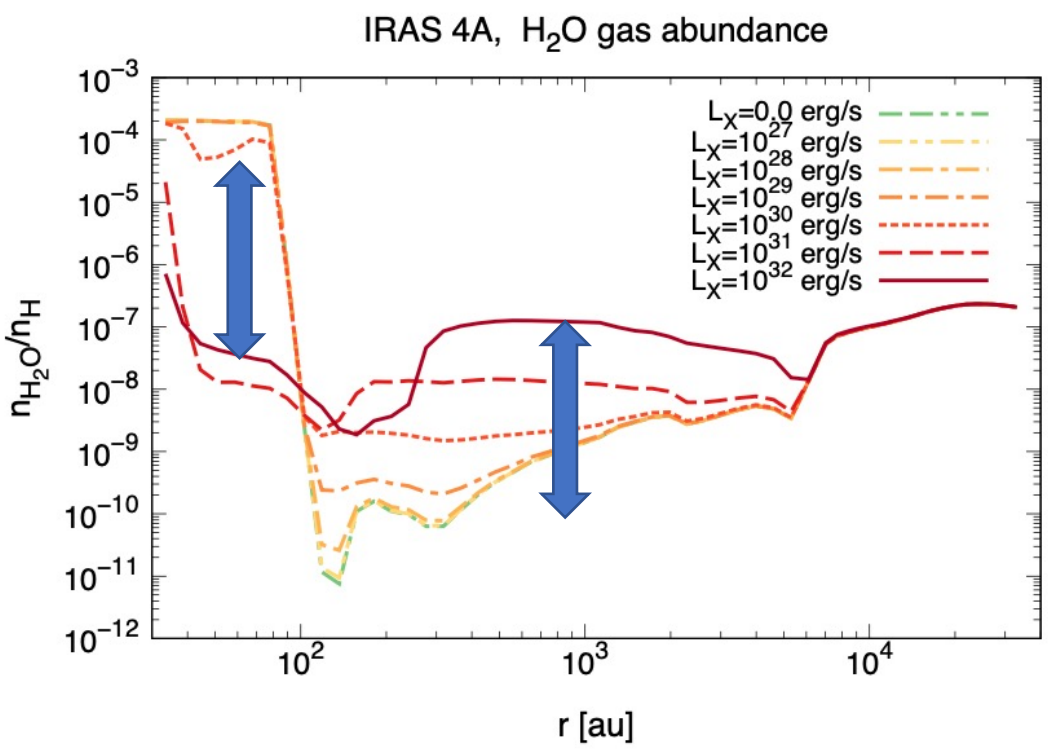

IRAS 4A model

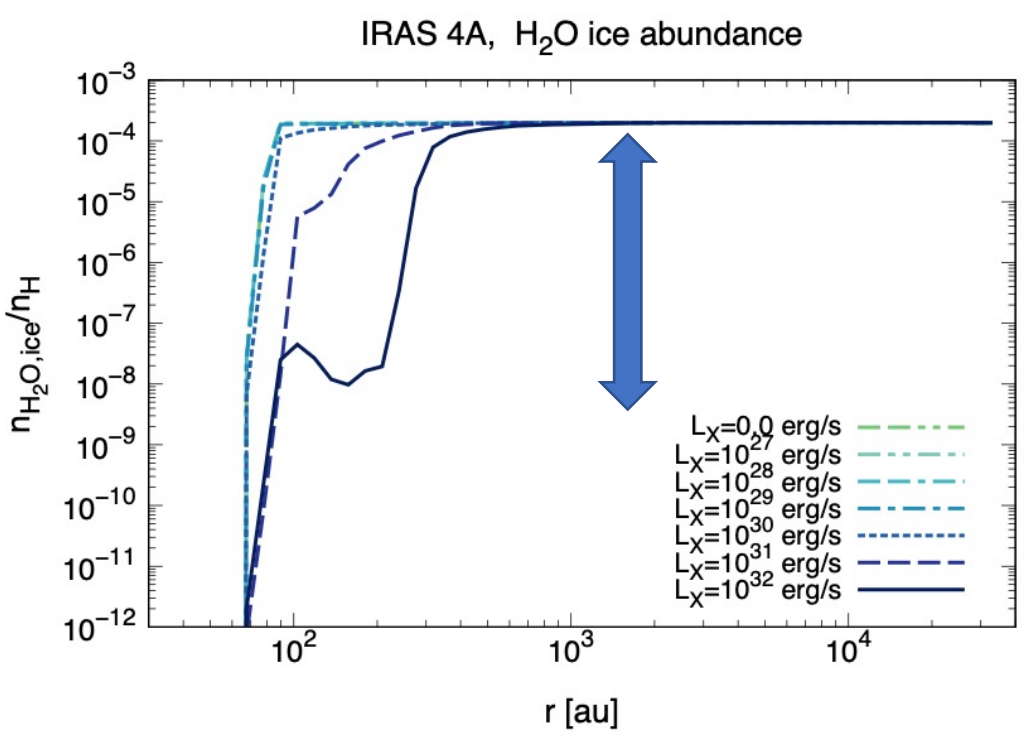

H_2Oスノーライン内側 ($<10^2$ au)：$L_X>10^{30}$ erg/s の時、H_2Oガス組成減少 ($10^{-4} \rightarrow 10^{-7}$-$10^{-6}$)
X線由来のイオン・分子反応(with H^+, H_3^+ etc.)や光解離反応(H+OH)が重要と考えられる

H_2Oスノーライン外側 ($>10^2$ au)： X線放射増大と共にH_2Oガス組成増加 ($10^{-10} \rightarrow 10^{-7}$)
X線由来の光脱離反応が重要と考えられる

低質量原始星エンベロープのO_2, O, COガス組成

Notsu et al. (2021)

IRAS 4A model

COガス組成：X線放射の影響をほぼ受けない

O_2, Oガス組成：X線放射増大 & H_2Oガス分子減少と共に増加
L_X>10^{30}-10^{31}erg/s の時、COと並んで酸素原子の主要な担い手に(~10^{-4})

COはt>1 Myr でdepletion →e.g., Bosman et al. (2018)

O_2: サブミリ波輝線は弱く、tentativeな検出例のみ
Herschel/HIFI: $^{16}O^{16}O$ 487 GHz (Yildiz et al. 2013) for IRAS 4A
ALMA: $^{16}O^{18}O$ 234 GHz (Taquet et al. 2018) for IRAS 16293-2422
O: ダスト光学的厚みが大きな遠赤外線に輝線が存在
↓
X線放射の影響を強く受ける、
(空間分解)観測が可能な分子とは?

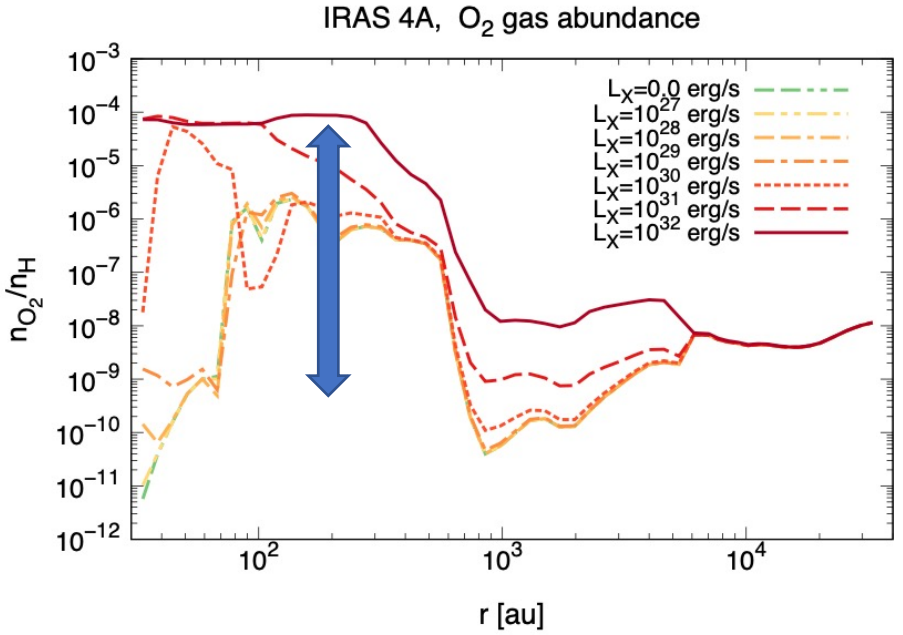

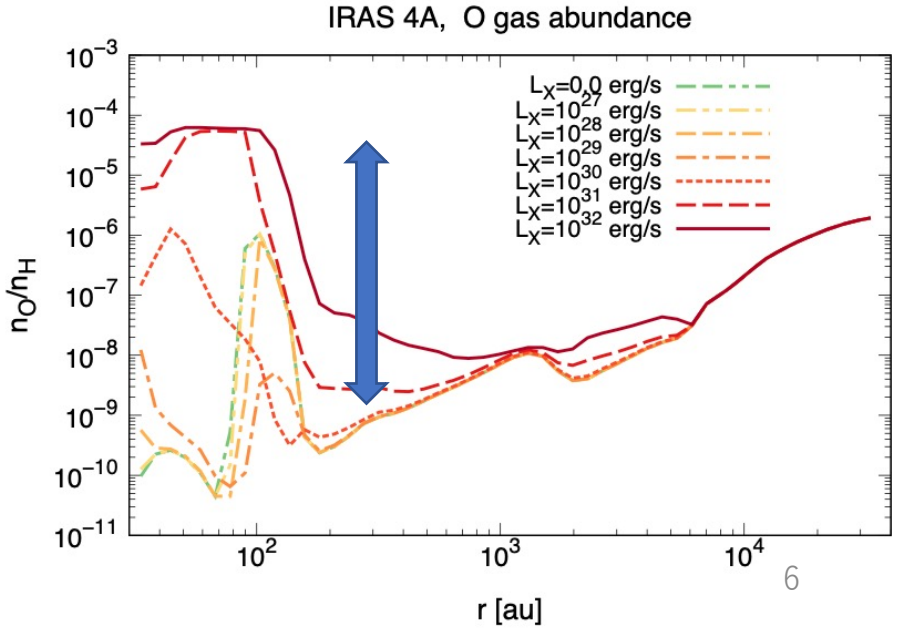

低質量原始星エンベロープのHCO⁺, CH_3OHガス組成

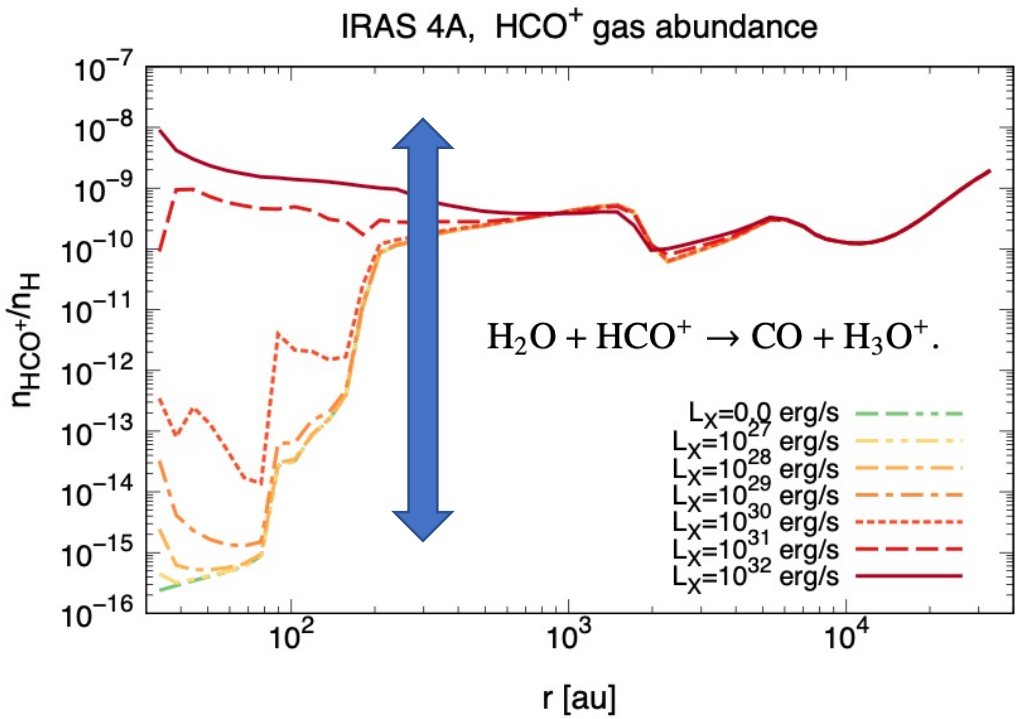

IRAS 4A model

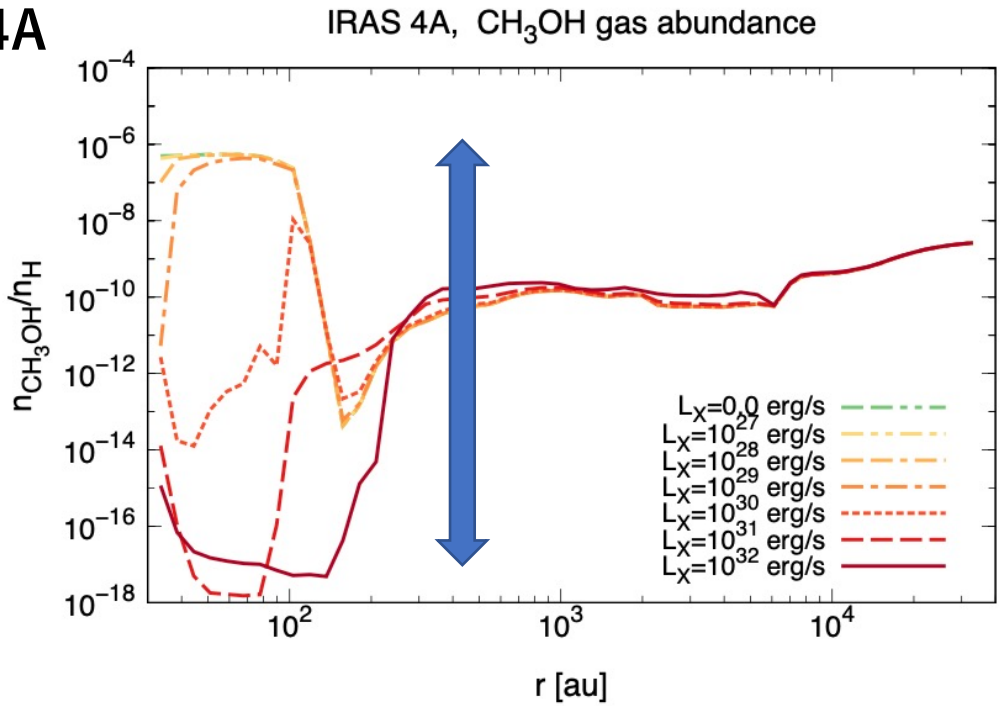

Notsu et al. (2021)

HCO⁺, CH_3OH: H_2O分子のトレーサーとして使われてきた

H_2Oスノーライン内側(r<100 au)において、$L_X>10^{30\text{-}31}$erg/s の時、
HCO⁺ガス組成増加 (H_2Oガス減少に伴う)、CH_3OHガス組成減少

↓

$L_X>10^{30\text{-}31}$erg/s の時、H_2Oスノーラインはトレーサーとして使用できない
一方でガス分布から、内縁の(X線)電離度ξ_Xや中心星X線光度L_Xなどの制約可能性あり

https://arxiv.org/abs/2103.08599v2

30. The double signature of local cosmic-ray acceleration in star-forming regions

Marco Padovani, Alexandre Marcowith, Daniele Galli, Leslie K. Hunt, Francesco Fontani ★

Recently, there has been an increased interest in the study of the generation of low-energy cosmic rays (CRs; < 1 TeV) in shocks situated on the surface of a protostar or along protostellar jets. These locally accelerated CRs offer an attractive explanation for the high levels of non-thermal emission and ionisation rate, ζ, observed close to these sources. The high ζ observed in some protostellar sources is generally attributed to shock-generated UV photons. The aim of this article is to show that when synchrotron emission and a high ζ are measured in the same spatial region, a locally shock-accelerated CR flux is sufficient to explain both phenomena. We assume that relativistic particles are accelerated according to the first-order Fermi acceleration mechanism and compute ζ and the non-thermal emission at cm wavelengths. We then apply our model to the star-forming region OMC-2 FIR 3/FIR 4. Using a Bayesian analysis, we constrain the parameters of the model and estimate the spectral indices of the non-thermal radio emission. We demonstrate that the local CR acceleration model makes it possible to simultaneously explain the synchrotron emission along the HOPS 370 jet within the FIR 3 region and ζ observed near the FIR 4 protocluster. Our model constrains the magnetic field strength (250-450 μG), its turbulent component (20-40 μG), and the jet velocity in the shock reference frame for the three non-thermal sources of the HOPS 370 jet (350-1000 km s^{-1}). Beyond the modelling of the OMC-2 FIR 3/FIR 4 system, we show how the combination of continuum observations at cm wavelengths and molecular transitions is a powerful new tool for the analysis of star-forming regions: these two types of observations can be simultaneously interpreted by invoking only the presence of locally accelerated CRs, without having to resort to shock-generated UV photons.

-原始星周囲の高い電離率(※)：従来、(jet内や原始星表面の)衝撃波で生成されたUV光子が要因とされてきた。
-本研究：衝撃波での宇宙線(<1TeV)加速が、高電離率とシンクロトロン放射の双方を説明可能であると提案。星形成領域モデル計算を実施。OMC-2 FIR 3/FIR 4 の観測との比較も行い、cm連続波と分子輝線観測の重要性を議論。

※ 主にHerschel & 単一鏡による$r>10^3$ au (エンベロープ全体)スケールの分子輝線観測で、高い電離率の値(一部の天体で$\xi \sim 10^{-14}$ s^{-1}) が観測された。(⇄X線による電離は主に中心星近傍($<<10^3$ au)に寄与)

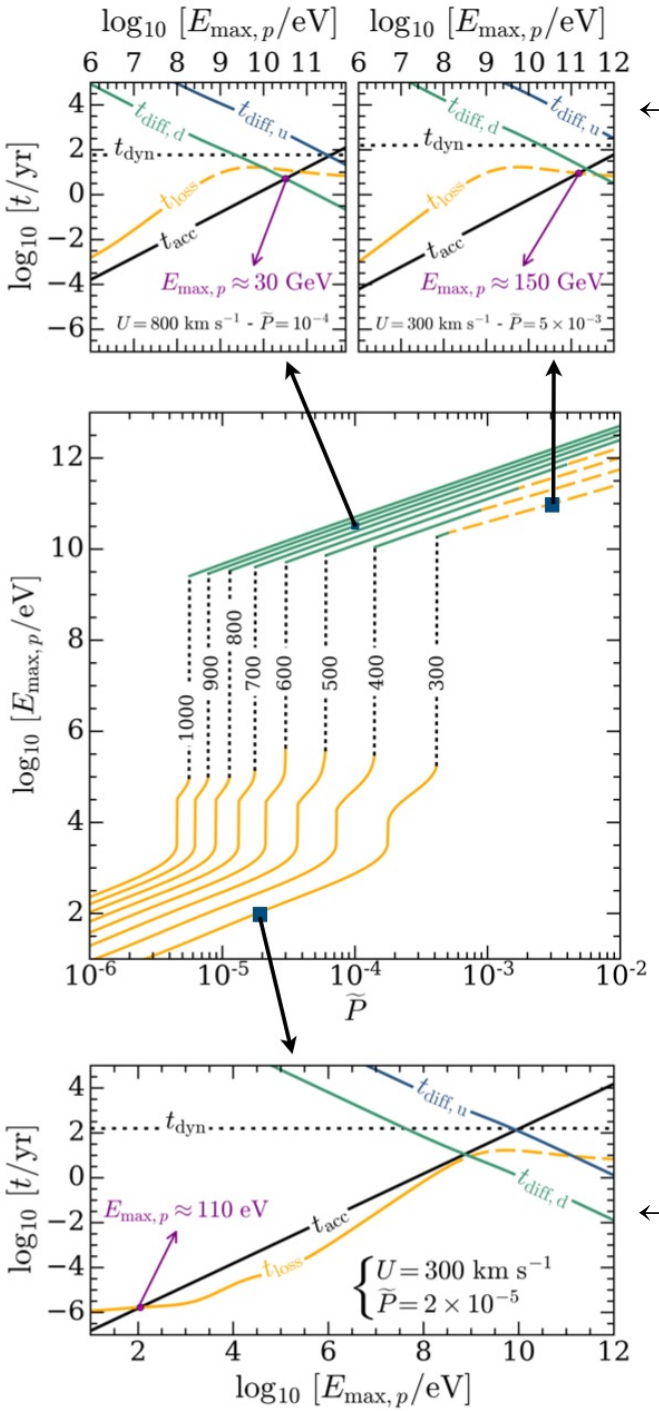

← t_{acc} vs t_{diff}で$E_{max,p}$が決まる

衝撃波内での加速・散逸・衝撃波の拡散のタイムスケール

$$t_{\mathrm{acc}} = 1.2 \times 10^{-2} k_{\mathrm{u}} (\gamma - 1) \frac{\varrho(\varrho+1)}{\varrho - 1} \left(\frac{U}{500\ \mathrm{km\ s^{-1}}} \right)^{-2} \left(\frac{B}{100\ \mu\mathrm{G}} \right)^{-1} \tag{3}$$

$$t_{\mathrm{loss}} = 10 \frac{\gamma - 1}{\beta} \left(\frac{n}{10^6\ \mathrm{cm^{-3}}} \right)^{-1} \left(\frac{L}{10^{-16}\ \mathrm{eV\ cm^2}} \right), \tag{4}$$

$$t_{\mathrm{diff,u}} = \frac{2.3 \times 10^4}{k_{\mathrm{u}} \gamma \beta^2} \left(\frac{B}{100\ \mu\mathrm{G}} \right) \left(\frac{R}{10^3\ \mathrm{AU}} \right) \left[\frac{\min(\ell_\perp, \epsilon R)}{10^3\ \mathrm{AU}} \right], \tag{5}$$

$$t_{\mathrm{diff,d}} = \frac{5.7 \times 10^3}{k_{\mathrm{u}} \gamma \beta^2} \left(\frac{B}{100\ \mu\mathrm{G}} \right) \left(\frac{\ell_\perp}{10^3\ \mathrm{AU}} \right)^2, \tag{6}$$

$$t_{\mathrm{dyn}} = 9.4 \left(\frac{R}{10^3\ \mathrm{AU}} \right) \left(\frac{U}{500\ \mathrm{km\ s^{-1}}} \right)^{-1}, \tag{7}$$

←加速された粒子の圧力 vs 陽子の最大エネルギー$E_{max,p}$
図中の数字はjetの速度U [km/s]

← t_{acc} vs t_{loss}で$E_{max,p}$が決まる

シンクロトロン放射のモデルfitting

Table 1. Parameters from model fitting[a].

Source	χ^2	U [km s^{-1}]	$\log_{10}\widetilde{P}$	B [μG]	n [10^6 cm^{-3}]	$\ell_\perp$ [AU]
		Ranges of uniform priors				
		$[300, 1000]$	$[-6, -2]$	$[10^2, 10^4]$	$[0.8, 2]$	$[100, 400]$
		Posteriors[b]				
VLA 12N	0.09	1000^{+0}_{-350}	$-4.70^{+0.33}_{-0.61}$	242^{+103}_{-72}	$0.82^{+0.41}_{-0.00}$	100
VLA 12C	1.36	1000^{+0}_{-250}	$-4.85^{+0.27}_{-0.45}$	438^{+150}_{-92}	$1.23^{+0.43}_{-0.31}$	100
VLA 12S	3.03	350^{+350}_{-50}	$-4.76^{+0.82}_{-0.54}$	367^{+221}_{-124}	$0.91^{+0.45}_{-0.09}$	400

[a] The temperature is fixed to 10^4 K and the ionisation fraction to 1.
[b] These values correspond to the mode of the PDF and a percentile range between 16% and 84% (i.e. a $\pm1\sigma$ spread assuming Gaussian errors).

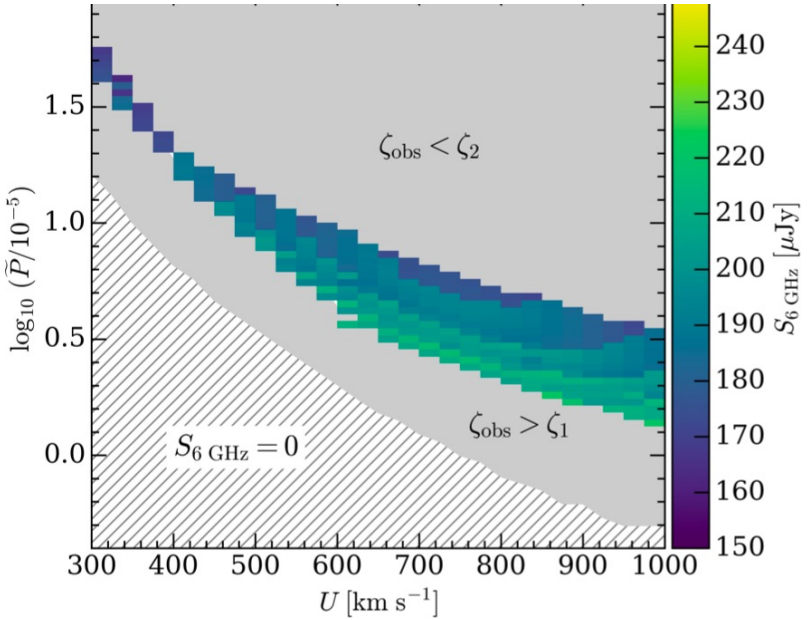

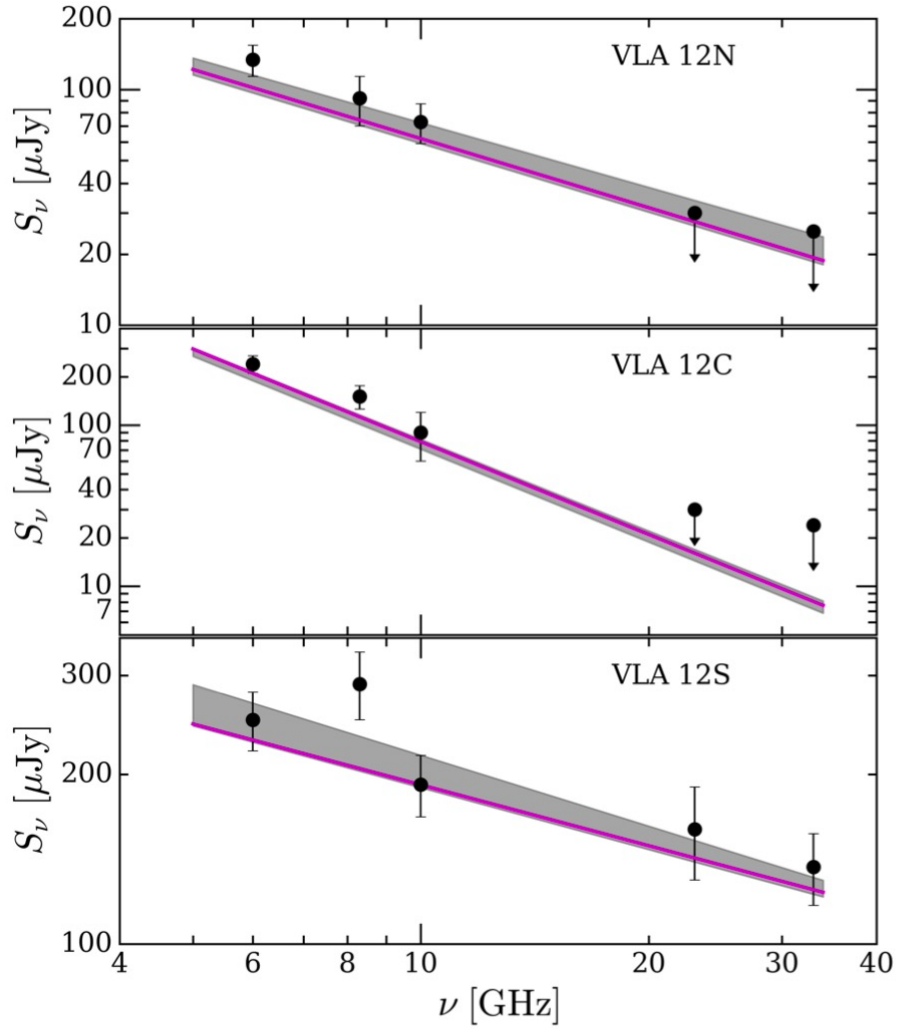

Fig. 6. Comparison between the observed flux densities (solid black circles; Osorio et al. 2017; Tobin et al. 2019) and the best-fit models (solid magenta lines) for the three knots, VLA 12N, 12C, and 12S. The grey shaded areas encompass the models within a confidence interval between 50% (second quartile) and 96% (2σ).

https://arxiv.org/abs/2104.06845v1

32. Significant interstellar object production by close stellar flybys

Susanne Pfalzner, Luis Aizpuru Vargas, Asmita Bhandare, Dimitri Veras ★ Within just two years, two interstellar objects (ISOs) - Oumuamuas and Borisov - have been discovered. Large quantities of planetesimals form as a by-product of planet formation. Therefore, it seems likely that ISOs are former planetesimals that became unbound from their parent star. The discoveries raise the question of the dominant ISO formation process. Here, we concentrate on planetesimals released during another star's close flybys. We quantify the amount of planetesimals released during close stellar flybys, their ejection velocity and likely composition. We study the dependence of the effect of parabolic flybys on the mass ratio between the perturber and parent star, the periastron distance, inclination, and angle of periastron. Whenever ISOs are produced, they leave their parent system typically with velocities of 0.5-2 km/s. This ejection velocity is distinctly different to that of ISOs produced by planet scattering (4-8 km/s) and those shed during the stellar post-main-sequence phase 0.1-0.2 km/s). Using the typical disc truncation radius in various cluster environments, we find that clusters like the Orion nebula cluster are likely to produce the equivalent of 0.85 Earth-masses of ISOs per star. In contrast, clusters like NGC 3603 could produce up to 50 Earth-masses of ISOs per star. Our solar system probably produced the equivalent of 2-3 Earth masses of ISOs, which left our solar system at a mean ejection velocity of 0.7 km/s. Most ISOs produced by flybys should be comet-like, similar to Borisov. ISOs originating from compact long-lived clusters would often show a deficiency in CO. As soon as a statistically significant sample of ISOs is discovered, the combined information of their observed velocities and composition might help in constraining the dominant production process (abridged).

この2年の間に、星間空間由来の天体(ISO)が2つ(1I/'Oumuamuaと2I/Borisov)も発見。その頻度等に関心。
本研究：放物線状の近星遭遇(flyby)を考え、天体間の質量や距離、角度などを様々に変えた数値計算を実施。
　　獲得される微惑星の量や入射速度、組成などを調査。
結果：ISOsの組成はcomet-likeがdominant, ('OumuamuaよりはBorisovに組成が近い)
　　大質量星への巡行遭遇が最も多くのISOを供給する。例えば5太陽質量星への250 au以内の遭遇では、
　　母天体に重力束縛され続ける質量より、微惑星として供給される質量の方が多くなる．etc.

Table 1: Simulation parameter space.

Parameter		Value
M_{21}		0.3, 0.5, 0.75, 1, 1.5, 2, 5, 10, 20, 50
r_p	[AU]	80, 100, 120, 140, 160, 200, 250, 350
i	[°]	0, 30, 60, 70, 80, 90, 120, 150, 180
ω	[°]	0, 15, 30, 45, 60, 70, 90

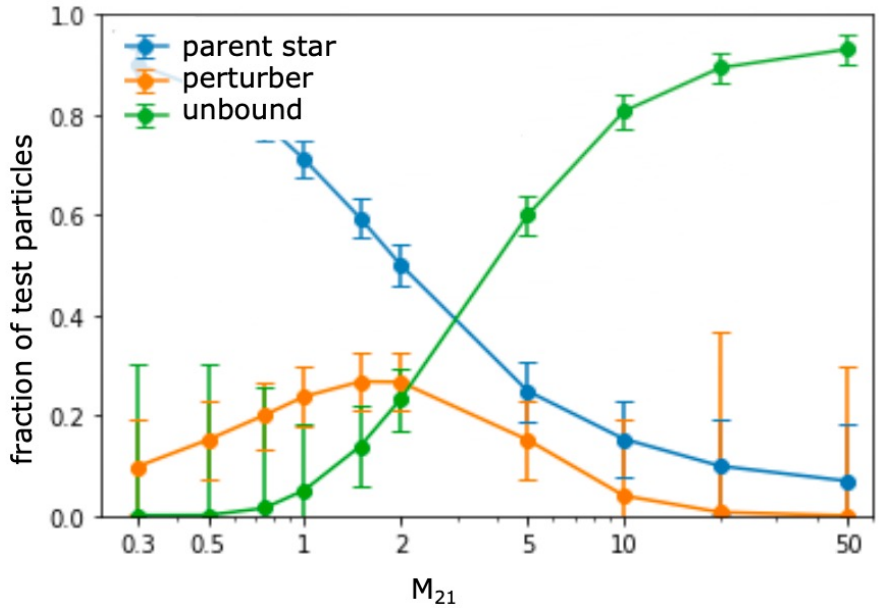

Fig. 3: Fraction of test particles remaining bound to the parent star (blue), being captured by the perturber (orange) and becoming unbound (green) as a function of perturber mass for a flyby with a periastron distance of 160 AU.

大質量星への巡行遭遇ほど、より多くのISOを供給する

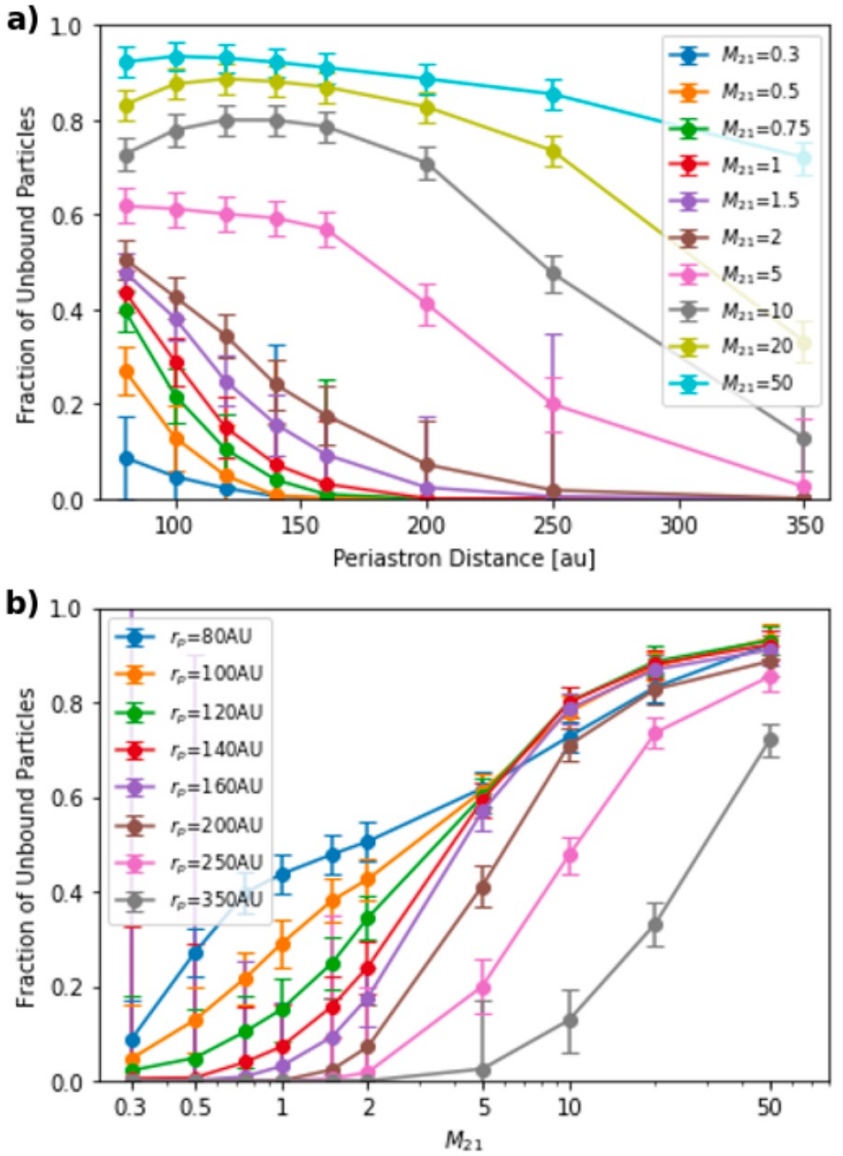

Fig. 4: Fraction of unbound test particles as a function of (a) periastron distance and (b) different stellar mass ratios.

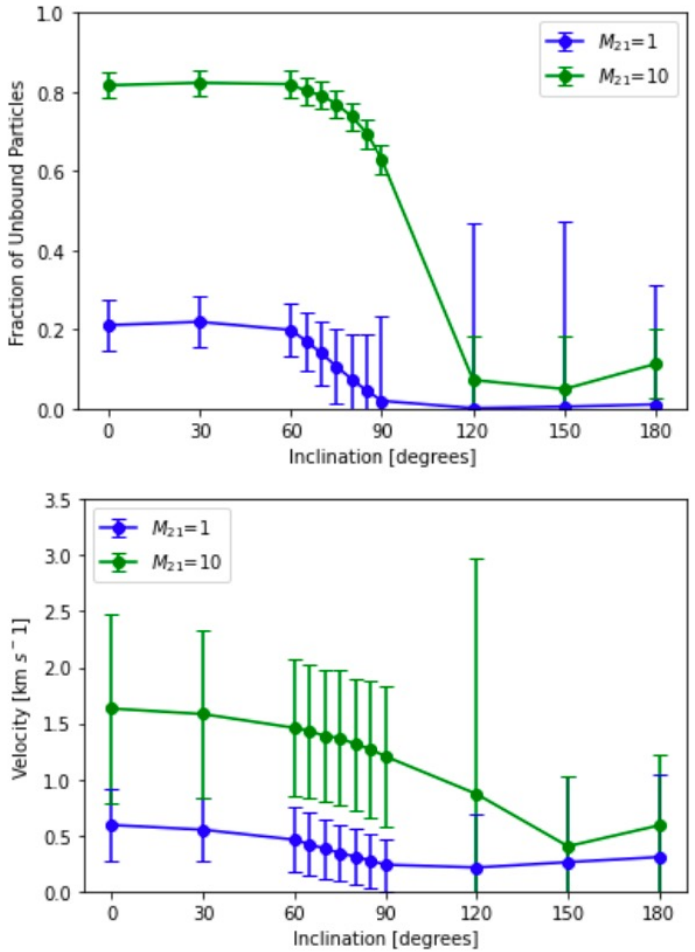

Fig. 7: The effect of inclination on the ISO production. The periastron distance in all cases was r_p =120 AU. The top panel a) shows the percentage of planetesimals becoming unbound and the bottom panel b) their mean velocity as a function of the inclination. Both properties are displayed for M_{21} = 1 (blue line) and M_{21} = 10 (green line). The inclination is given in degrees.

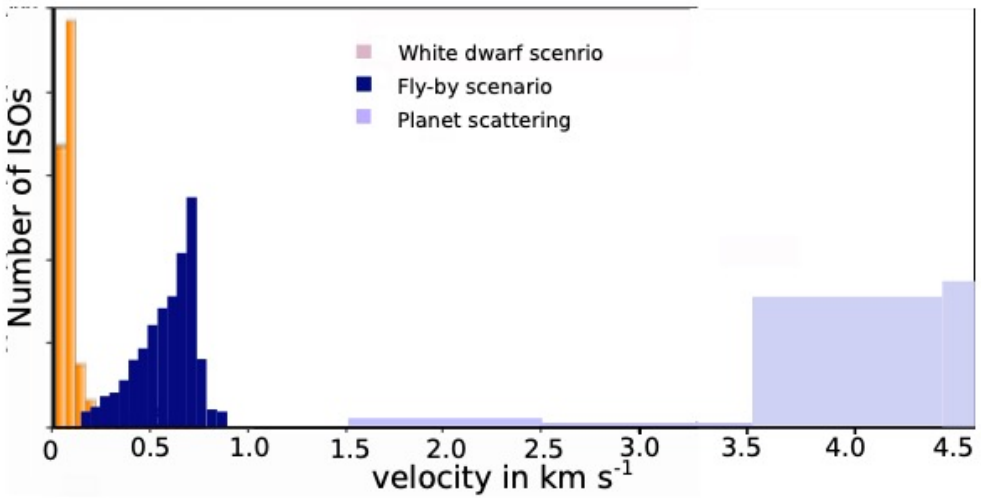

Fig. 8: Comparison of the ejection velocity distributions of ISOs produced during the post-main sequence phase (unpublished material based on Veras et al. 2014b, orange), the flyby scenario computed here (dark blue) and during the planet scattering phase (adapted from Adams & Spergel 2005, light blue). The last is only partly shown, it extends further to the higher values. The velocity bin width is 0.05 km s^{-1} for the flyby and post-main sequence scenario and 1 km s^{-1} for the planet scattering case.

大質量星への巡行遭遇ほど、より多くのISOを供給する

https://arxiv.org/abs/2103.12644v2

34. The effect of the streaming instability on protoplanetary disc emission at millimetre wavelengths

Chiara E. Scardoni, Richard A. Booth, Cathie J. Clarke ★
In this paper, we investigate whether overdensity formation via streaming instability is consistent with recent multi-wavelength ALMA observations in the Lupus star forming region. We simulate the local action of streaming instability in 2D using the code ATHENA, and examine the radiative properties at mm wavelengths of the resulting clumpy dust distribution by focusing on two observable quantities: the optically thick fraction ff (in ALMA band 6) and the spectral index α (in bands 3-7). By comparing the simulated distribution in the $ff-\alpha$ plane before and after the action of streaming instability, we observe that clump formation causes ff to drop, because of the suppression of emission from grains that end up in optically thick clumps. α, instead, can either increase or decline after the action of streaming instability; we use a simple toy model to demonstrate that this behaviour depends on the sizes of the grains whose emission is suppressed by being incorporated in optically thick clumps. In particular, the sign of evolution of α depends on whether grains near the opacity maximum at a few tenths of a mm end up in clumps. By comparing the simulation distributions before/after clump formation to the data distribution, we note that the action of streaming instability drives simulations towards the area of the plane where the data are located. We furthermore demonstrate that this behaviour is replicated in integrated disc models provided that the instability is operative over a region of the disc that contributes significantly to the total mm flux.

ストリーミング不安定により生成される高密度(=光学的に厚い)構造が、Lupus領域の円盤のALMA多波長連続波観測の結果(Tazzari et al. 2020a, b)とconsistentかどうかを調査。
観測可能な物理量としてff (Band 6での光学的厚みの割合)とspectral index α (Bands 3-7)に着目し、ストリーミング不安定によるclumpの生成前・後でシミュレーション(by Athena)の値と観測値を比較

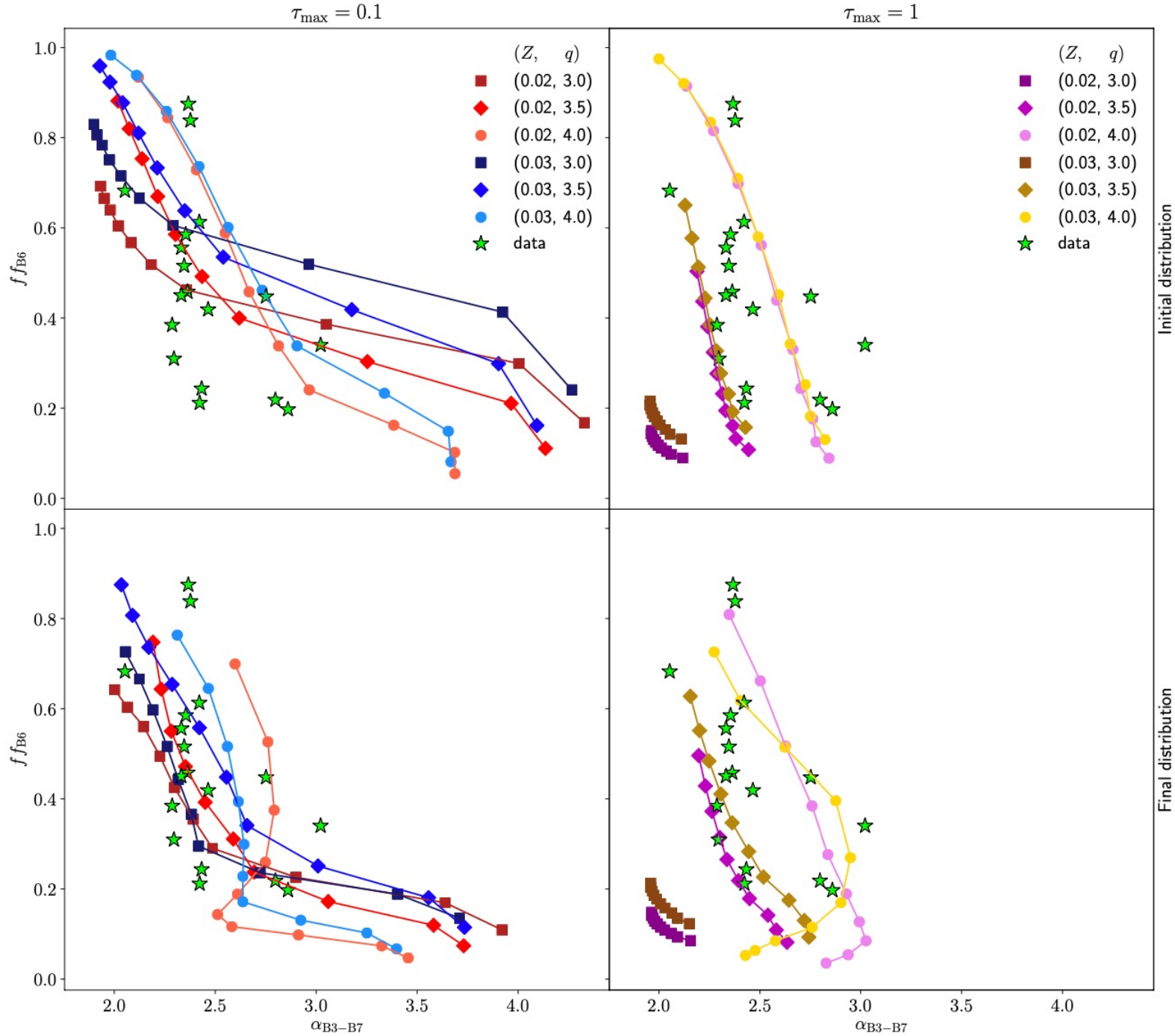
$\tau_{\max} = 0.1$
$\tau_{\max} = 1$
$(Z,\ q)$
(0.02, 3.0)
(0.02, 3.5)
(0.02, 4.0)
(0.03, 3.0)
(0.03, 3.5)
(0.03, 4.0)
data
$f\,f_{\rm B6}$
$\alpha_{\rm B3-B7}$
Initial distribution
Final distribution

https://arxiv.org/abs/2104.02597v1

27. Magnetic Properties of Star-Forming Dense Cores

Philip C. Myers, Shantanu Basu ★

Magnetic and energetic properties are presented for 17 dense cores within a few hundred pc of the Sun. Their plane-of-sky field strengths are estimated from the dispersion of polarization directions, following Davis, Chandrasekhar and Fermi (DCF). Their ratio of mass to magnetic critical mass is 0.5-3, indicating nearly critical field strengths. The field strength B_{pos} is correlated with column density N as $B_{pos} \sim N^p$, where p=1.05±0.08, and with density n as $B_{pos} \sim n^q$, where q=0.66±0.05. These magnetic properties are consistent with those derived from Zeeman studies (Crutcher et al. 2010), with less scatter. Relations between virial mass M_V, magnetic critical mass M_B, and Alfven amplitude $sigma_B$/B match the observed range of M/M_B for cores observed to be nearly virial, with M/M_V=0.5-2, with moderate Alfven amplitudes, and with $sigma_B$/B=0.1-0.4. The B-N and B-n correlations in the DCF and Zeeman samples can be explained when such bound, Alfvenic, and nearly-critical cores have central concentration and spheroidal shape. For these properties, B N because M/M_B is nearly constant compared to the range of N, and $B \sim n^{2/3}$ because $M^{1/3}$ is nearly constant compared to the range of $n^{2/3}$. The observed core fields which follow $B \sim n^{2/3}$ need not be much weaker than gravity, in contrast to core fields which follow $B \sim n^{2/3}$ due to spherical contraction at constant mass (Mestel 1966). Instead, the nearly critical values of M/M_B suggest that the observed core fields are nearly as strong as possible, among values which allow gravitational contraction.

DCF: Alfvén波が励起する乱流により偏光ベクトルの方向が統計的に変動する現象を利用し、平面上の磁場強度を測定する手法。
本研究：17個のコアに対し、DCFとZeeman見積もった磁場強度などを比較、Mass/Flux比や、密度依存性などを議論。

$$B_{\mathrm{pos}} = Q(4\pi\rho)^{1/2}\sigma_{NT}\sigma_{\theta}^{-1} \qquad (1)$$

https://arxiv.org/abs/2102.08564v1

28. Testing the Turbulent Origin of the Stellar Initial Mass Function

D. G. Nam, C. Federrath, M. R. Krumholz ★
Supersonic turbulence in the interstellar medium (ISM) is closely linked to the formation of stars, and hence many theories connect the stellar initial mass function (IMF) with the turbulent properties of molecular clouds. Here we test three turbulence-based IMF models (by Padoan & Nordlund 2002, Hennebelle & Chabrier 2008, and Hopkins 2012), which predict the relation between the high-mass slope (Γ) of the IMF, $\mathrm{d}N/\mathrm{d}\log M \propto M^{\Gamma}$ and the exponent n of the velocity power spectrum of turbulence, $E_v(k) \propto k^{-n}$, where $n \approx 2$ corresponds to typical ISM turbulence. Using hydrodynamic simulations, we drive turbulence with an unusual index of $n \approx 1$, measure Γ, and compare the results with $n \approx 2$. We find that reducing n from 2 to 1 primarily changes the high-mass region of the IMF (beyond the median mass), where we measure high-mass slopes within the 95 per cent confidence interval of $-1.5 < \Gamma < -1$ for $n \approx 1$ and $-3.7 < \Gamma < -2.4$ for $n \approx 2$, respectively. Thus, we find that $n = 1$ results in a significantly flatter high-mass slope of the IMF, with more massive stars formed than for $n \approx 2$. We compare these simulations with the predictions of the three IMF theories. We find that while the Padoan & Nordlund theory matches our simulations with fair accuracy, the other theories either fail to reproduce the main qualitative outcome of the simulations or require some modifications. We conclude that turbulence plays a key role in shaping the IMF, with a shallower turbulence power spectrum producing a shallower high-mass IMF, and hence more massive stars.

流体力学乱流下の分子雲内での星形成過程をAMR codeで数値計算。IMF(初期質量関数)の高質量側の傾きΓと、乱流速度場のパワースペクトルのペキnとの関係を比較。
n=2が通常の星間空間乱流場であるが、n~1とした場合のΓの値を調査。

n~2の場合$-1.5<\Gamma<1$, n~1の場合$-3.7<\Gamma<-2.4$となり、n~1の方がより大質量星に富む分布となる。

$$\mathrm{d}N/\mathrm{d}\log M \propto M^{\Gamma}$$

$$E_v(k) \propto k^{-n}$$

https://arxiv.org/abs/2104.00433v1

31. Modulated accretion in T Tauri star RY Tau – stable MHD propeller or a planet at 0.2 AU?

P. P. Petrov, M. M. Romanova, K. N. Grankin, S. A. Artemenko, E. V. Babina, S. Yu. Gorda

★ Planets are thought to form at the early stage of stellar evolution when the mass accretion is still ongoing. RY Tau is a T Tauri type star at the age of a few Myr, with accretion disc seen at high inclination, so that line of sight crosses both the wind and the accretion gas flows. In a long series of spectroscopic monitoring of the star in 2013-2020, we detected variations in H-alpha and NaI D absorptions at radial velocities of infall (accretion) and outflow (wind) with a period of about 22 days. The absorptions in the infalling and the outflowing gas streams vary in anti-phase: an increase of infall is accompanied by a decrease of outflow, and vice versa. These flip-flop oscillations retain phase over several years of observations. We suggest that this may result from the MHD processes at the disk-magnetosphere boundary in the propeller mode. Another possibility is that a massive planet modulates some processes in the disc and provides the observed effects. The period, if Keplerian, corresponds to a distance of 0.2 AU, which is close to the dust sublimation radius in this star. The presence of the putative planet may be confirmed by radial velocity measurements: expected amplitude is > 90 m/s if a planet mass is > 2 Mj.

T Tauri型星 RY Tauに対し、Hα線とNa I D線で分光モニター観測を7年間に亘り実施。22日周期で吸収線の視線速度変動(infall⇄outflow)を検出。
円盤-磁気圏境界面でのMHD降着 または 0.2 auに存在する惑星による変動 という2説を議論。

https://arxiv.org/abs/2104.08036v2

33. Thiols in the ISM: first detection of HC(O)SH and confirmation of C_2H_5SH

Lucas F. Rodríguez-Almeida, Izaskun Jiménez-Serra, Víctor M. Rivilla, Jesús Martín-Pintado, Shaoshan Zeng, Belén Tercero, Pablo de Vicente, Laura Colzi, Fernando Rico-Villas, Sergio Martín, Miguel A. Requena-Torres

★ The chemical compounds carrying the thiol group (-SH) have been considered essential in recent prebiotic studies regarding the polymerization of amino acids. We have searched for this kind of compounds toward the Galactic Centre quiescent cloud G+0.693-0.027. We report the first detection in the interstellar space of the trans-isomer of monothioformic acid (t-HC(O)SH) with an abundance of $\sim 1 \times 10^{-10}$. Additionally, we provide a solid confirmation of the gauche isomer of ethyl mercaptan (g-C_2H_5SH) with an abundance of $\sim 3 \times 10^{-10}$, and we also detect methyl mercaptan (CH_3SH) with an abundance of $\sim 5 \times 10^{-9}$. Abundance ratios were calculated for the three SH-bearing species and their OH-analogues, revealing similar trends between alcohols and thiols with increasing complexity. Possible chemical routes for the interstellar synthesis of t-HC(O)SH, CH_3SH and C_2H_5SH are discussed, as well as the relevance of these compounds in the synthesis of prebiotic proteins in the primitive Earth.

チオール基(-SH基)を含む化合物は、アミノ酸(システイン)の重合反応において重要。
IRAM 30m とYebes 40m 電波望遠鏡で、銀河中心方向の星間雲G+0.693-0.027の分光スペクトルサーベイを実施。
モノチオギ酸のトランス異性体(t-HC(O)SH)を星間空間で初検出 。そのほか、CH_3SHとC_2H_5SHなども検出。

https://arxiv.org/abs/2103.07922v2

35. Gaia-EDR3 Parallax Distances to the Great Carina Nebula and its Star Clusters (Trumpler 14, 15, 16)

Michael Shull, Jeremy Darling, Charles Danforth ★ Using offset-corrected Gaia-EDR3 parallax measurements and spectrophotometric methods, we have determined distances for 69 massive stars in the Carina OB1 association and associated clusters: Trumpler 16 (21 stars), Trumpler 14 (20 stars), Trumpler 15 (3 stars), Bochum 11 (5 stars), and South Pillars region (20 stars). Past distance estimates to the Carina Nebula range from 2.2 to 3.6 kpc, with uncertainties arising from photometry and anomalous dust extinction. The EDR3 parallax solutions show considerable improvement over DR2, with typical errors $\sigma_\varpi/\varpi \approx$ 3-5Great Carina Nebula lie at essentially the same distance (2.35 ± 0.08 kpc), quoting mean and rms variance. The clusters have distances of 2.32±0.12 kpc (Tr 16), 2.37±0.15 kpc (Tr 14), 2.36±0.09 kpc (Tr 15), and 2.33±0.12 kpc (Bochum 11) in good agreement with the η Car distance of around 2.3 kpc. O-star proper motions suggest internal (2D) velocity dispersions ~ 4 km/s for Tr 14 and Tr 16. Reliable distances allow estimates of cluster sizes, stellar dynamics, luminosities, and fluxes of photoionizing radiation incident on photodissociation regions in the region. We estimate that Tr 14 and Tr 16 have half-mass radii $r_h = 1.5 - 1.8$ pc, stellar crossing times $t_{\rm cr} = r_h/v_m \approx 0.7 - 0.8$ Myr, and two-body relaxation times $t_{rh} \approx 40 - 80$ Myr. The underlying velocity dispersion for Tr 14, if a bound cluster, would be $v_m \approx 2.1^{+0.7}_{-0.4}$ km/s for $N = 7600^{+5800}_{-2600}$ stars. With the higher dispersions of the O-stars, mass segregation might occur slowly, on times scales of 3-6 Myr.

Gaiaの新しいデータリリース Gaia-EDR3の年周視差の値を用いて、Carina OB1 associationとその付属星団にある69個の大質量星の距離をupdate.